Journal of Geochemical Exploration 185 (2018) 105–115

Contents lists available at ScienceDirect

Journal of Geochemical Exploration

journal homepage: www.elsevier.com/locate/gexplo

Hydrogeological and hydrogeochemical study of a volcanic-sedimentary coastal aquifer in the archaeological site of Cumae (Phlegraean Fields, southern Italy)

Vincenzo Allocca[a], Silvio Coda[a], Pantaleone De Vita[a], Brunella Di Rienzo[d], Luciano Ferrara[b], Antonella Giarra[b], Olga Mangoni[c], Luisa Stellato[d], Marco Trifuoggi[b], Michele Arienzo[a,*]

[a] Dipartimento di Scienze della Terra, dell'Ambiente e delle Risorse, Università degli Studi di Napoli Federico II, Complesso Universitario di Monte S. Angelo, via Cintia, 80126 Naples, Italy
[b] Dipartimento di Scienze Chimiche, Università degli Studi di Napoli Federico II, Complesso Universitario di Monte S. Angelo, via Cintia, 80126 Naples, Italy
[c] Dipartimento di Biologia, Università degli Studi di Napoli Federico II, Complesso Universitario di Monte S. Angelo, Via Cintia, 80126 Naples, Italy
[d] Centre for Isotopic Research on Cultural and Environmental Heritage (CIRCE), Dipartimento di Matematica e Fisica, Università degli Studi della Campania Luigi Vanvitelli, Caserta, Italy

ARTICLE INFO

Keywords:
Archaeological ruins
Hydrogeology
Hydrogeochemistry
^{222}Rn
Volcanic-sedimentary coastline aquifer
Cumae archaeological site

ABSTRACT

A hydrogeological and hydrogeochemical survey in the *Cumae* archaeological site (Phlegraean Fields, southern Italy) together with radon levels determination in groundwater have been carried out. The study was motivated by the fact that the site is often submerged by the outcrop of groundwater, threatening the integrity of ruins, and hence by the need to preserve such important archaeological park. The hydrostratigraphic and hydrogeological data revealed the presence of a multi-layered aquifer system, formed by a shallow unconfined and a deep semiconfined aquifer. The groundwater flow appeared to be strongly influenced by vertical and lateral lithological heterogeneity of volcanic-sedimentary deposits, as well as by groundwater pumping and drainage by surface micro-channel system. The dominant hydrochemical facies were Cl^--SO_4^{2-}-Na^+-K^+, HCO_3^--Ca^{2+}-Mg^{2+} and HCO_3^- Na^+-K^+ types. These facies were affected by: i) dissolution and chemical weathering, ion exchange with volcanic-sedimentary deposits, ii) localized rise along faults and fractured zones of deep magmatic fluids highly mineralized, with outstanding levels of F^-, 6.4 mg L^{-1} in deep water and 3.3 mg L^{-1} in shallow water, and ^{222}Rn, 31,500 Bq m^{-3} in deep water and 5400 Bq m^{-3} in shallow water; iii) freshwater-saltwater interactions, induced by groundwater pumping.

1. Introduction

The deterioration of in situ archaeological deposits (Holden et al., 2006) can be speeded by environmental and hydrogeological changes, caused by climate or land use changes. The conservation and management of organic and inorganic archaeological resources, especially in rural areas, is threatened by the use of fertilisers and pesticides, irrigations, ploughings and land drainage. Moreover, in active volcanic and coastal areas groundwater abstraction rates affect the chemistry of groundwater (Comte et al., 2016), salt-water intrusion (Bucci et al., 2011; Felisa et al., 2013) and the upwelling of highly mineralized deep fluids. This compromises state, conservation and preservation of in situ archaeological deposits (de Beer and Matthiesen, 2008). Therefore, in-depth knowledge of hydro-environmental systems and monitoring of hydrological and hydrochemical processes of the groundwater in the saturated and unsaturated soil zones represent a crucial prerequisite for the in situ preservation of archaeological remains (Holden et al., 2006; de Beer and Matthiesen, 2008).

The ancient city of *Cumae*, in the Naples Province, was the first Greek colony, named *Kyme*, founded in mainland southern Italy along the Tyrrhenian coast (Fig. 1a) in the 730 BCE, and remained continuously occupied until the 1207 CE (Boardman, 1995). Cumae hosts an important archaeological park, among the most important and visited of the southern Italy, located inside of the Phlegraean Fields Regional Park (Caputo et al., 1996).

The park includes different sites, artefact, cultural remains and ancient monuments, dating back to the Greek, Roman, and Byzantine epochs. In addition, along the north-west side of the city fortification, appears the Monumental Roman Necropolis, a small sub-flat coastal plain area used as burial environment in Roman period (Munzi and

* Corresponding author.
E-mail address: michele.arienzo@unina.it (M. Arienzo).

https://doi.org/10.1016/j.gexplo.2017.11.004
Received 11 May 2017; Received in revised form 11 October 2017; Accepted 9 November 2017
Available online 11 November 2017
0375-6742/

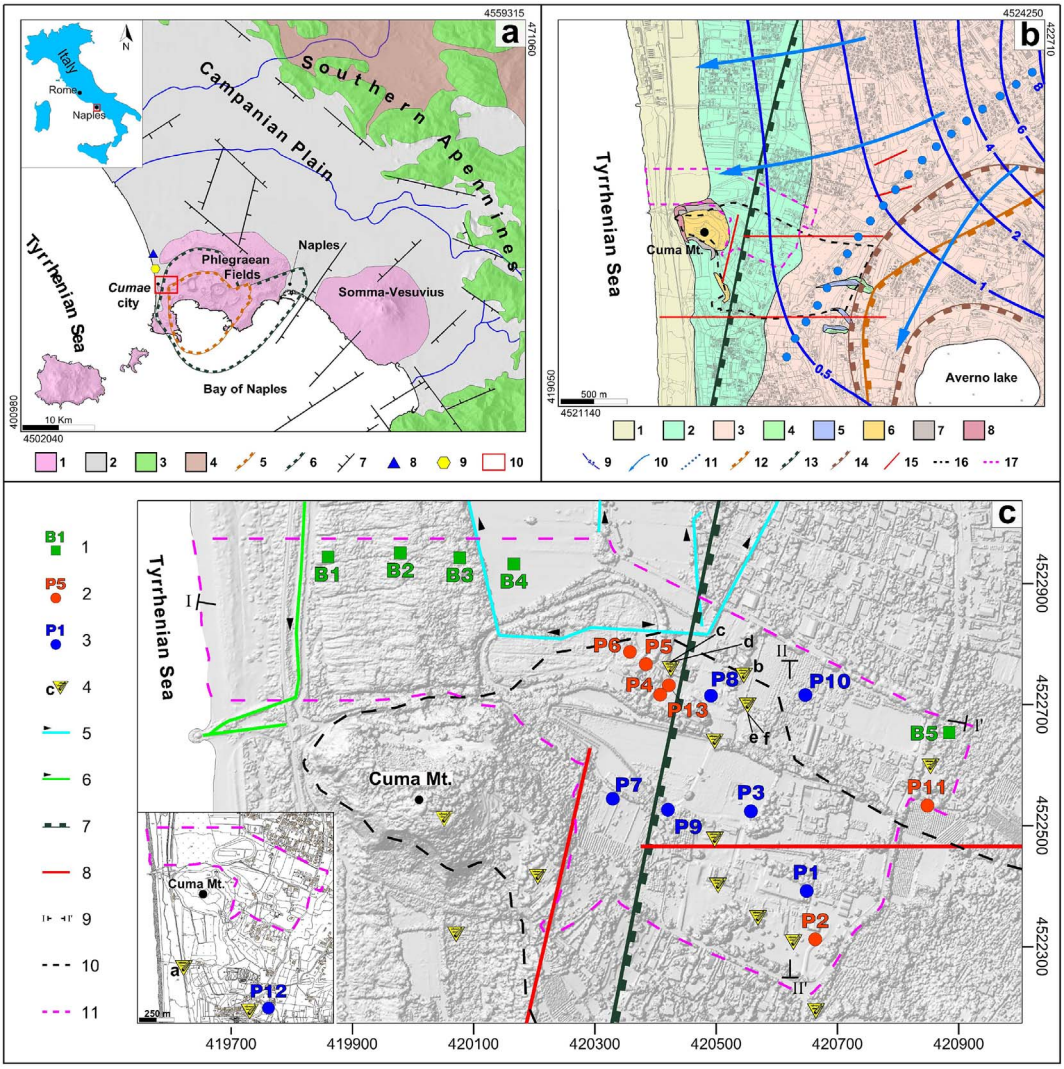

Fig. 1. a) Geological map of the Campanian Plain. 1) Quaternary epiclastic deposits; 2) Quaternary volcanic deposits; 3) Apennine platform carbonates; 4) Miocene deposits; 5) NYT caldera boundary; 6) CI caldera boundary; 7) Normal fault; 8) Licola pluviometric station; 9) Licola draining station; 10) Study area. b) Hydrogeological map of the western sector of Phlegraean Fields volcanic system. 1) Eolic deposits; 2) Pyroclastic-fluvio-palustrine deposits; 3) Pyroclastic deposits; 4) Baia's tuffs; 5) Gauro's eruption deposits; 6) Neapolitan Yellow Tuff; 7) Museum Breccia; 8) Mt. Cuma's lavas; 9) Groundwater contour line (m a.s.l.); 10) Groundwater flow direction; 11) Groundwater divide; 12) NYT caldera boundary; 13) CI caldera boundary; 14) Buried caldera boundary; 15) Normal fault; 16) Cumae archaeological park; 17) Study area. c) Groundwater monitoring network. 1) Borehole; 2) Shallow-well; 3) Deep-well; 4) Archaeological site; 5) Groundwater draining channel; 6) Waste water channel; 7) CI caldera boundary; 8) Normal fault; 9) Hydrogeological section; 10) Cumae archaeological park; 11) Study area.

Brun, 2011). In this site, archaeological researches have been conducted since 1809, and still continue, although the Roman Necropolis of *Cumae* was already known in the seventeenth century (Munzi and Brun, 2011; Birolo et al., 2016). However, in the last years, the archaeological researches have suffered a sharp slowdown and some inorganic archaeological materials, as burial chamber, have been reburied. This was due to rising of groundwater, as observed in other coastal plains of the southern Italy (Allocca and Celico, 2008; Allocca et al., 2016) and archaeological sites of the Mediterranean region (Abdallah and Ebd El-Tawab, 2013). The main causes of these processes have to be attributed to deterioration of the local drainage channel system, rising of sea levels from Roman period to the present in the central Mediterranean area (Lambeck et al., 2004) and local subsidence of the soil surface (Todesco et al., 2014). Thus, groundwater head up to + 1.20 m above the archaeological remains damaging structural and decorative elements (Fig. 2). Elevated emissions of radon are expected from the volcanic deposits and hence in the aquifer of the Cumae site, being part of the active volcanic system of Phlegraean Fields. Its transport can take place through the fissure network in the fractured system or from mantle degassing. In our study measurements of radon half-life and solubility (Cook et al., 2003; Stellato et al., 2008; Schubert et al., 2011; Stellato et al., 2013; Alonso et al., 2015) were used as a natural groundwater tracer to identify and quantify groundwater/surface waters interactions.

The main objectives of the study were to characterize the coastal volcanic-sedimentary aquifer system, determine the physical-chemical properties of the groundwater of *Cumae* site, and assess processes that control groundwater's geochemistry and its spatio-temporal evolution. The study was carried out through a multidisciplinary approach by a well-designed hydrogeological, hydrogeochemical, and isotopic surveys. The study represents a first original attempt to characterize this site and will help local authorities to adopt effective strategies for the preservation of the archaeological ruins.

2. Geological and hydrogeological features of the field research site

The *Cumae* archaeological site extends for about 3.0 km^2 along the

Fig. 2. Archaeological ruins impacted by water table rising. Location of the sites is in Fig. 1c. The photos a, b, d, e and f show signs of archaeological site-groundwater interactions (floods, capillary actions, colour alterations). The photo c and c' show water table fluctuations.

Tyrrhenian coast of the southern Italy, north-west of the active volcanic system of Phlegraean Fields, about 20 km north of Naples bay (Fig. 1a). The system occupies the center of Campanian Plain (Fig. 1a), a large alluvial plain, formed in the Pliocene-Pleistocene in a regional semi-graben structural depression of the southern Apennines (Cinque et al., 1993), and it is characterized by an intense volcanic activity starting from 300 ka (Rolandi et al., 2003). The calderic morphology of the volcanic system (Fig. 1b) is mainly originating from the superposition of two collapse episodes (Orsi et al., 1996) due to two large Pleistocene eruptions: Campanian Ignimbrite (CI) eruption dated 39 ka BP (De Vivo et al., 2001) and Neapolitan Yellow Tuff (NYT) eruption dated 15 ka BP (Deino et al., 2004). The Cuma site is located along the western edge of CI caldera boundaries (Fig. 1a), where several buried normal faults, fractures and deep crater rims (Fig. 1b and c) characterize this sector of the Phlegraean Field caldera (Bravi et al., 2003; Vitale and Isaia, 2014).

The *Cumae* archaeological site and its surrounding coastal plain are part of the Phlegraean Fields Regional Park and of the wetlands of the Phlegraean Area and Mount Cumae's Forest. During the Holocene period, this area was affected by endogenous and exogenous, natural and anthropogenic processes, such as volcanic eruption, bradyseismic crises, eustatic sea-level variations, shoreline changes, formation of lake environments and palustrine wetlands and land reclamation practices (since VI–V centuries B.C.) (Bravi et al., 2003; Stefaniuk et al., 2005).

The site is characterized by a complex volcanic-sedimentary sequence formed by sands, silts, silty clays and volcanoclastic sediments, overlying a substrate of consolidated yellow tuff and trachytic laves, breccias and welded scoria, outcropping in the surrounding relief of Cuma Mount (Fig. 1c). In this relief, constituting the wreck of an ancient volcanic building older than 39 ka age (Fig. 1b), the proximal facies of the CI formation, named Museum Breccia (Fedele et al., 2008), emerges. The latter geological formation is a welded deposit of ash and pumice thickness of about 1.5–2.0 m, along the eastern side of the NYT lithified facies. Outcrops of sands and silty sands, slightly thickened, and silts and clays deposits of marine and lagoon environment are evident in the coastal plain surrounding Cuma Mount (Fig. 1c). These deposits pass laterally into a depositional environment of volcanic sediments, as ash-fall pyroclastic deposits, stratified pumiceous lapillus and consolidated yellow tuffs.

The geomorphologic features are typical of a coastal plain, with altitude range of 0–15 m a.s.l., constituted, from the sea toward the inland, by beach-dune systems followed by a low inclination back-dune zone and slope areas belonging to volcanic reliefs. The flat morphology of the coastal plain is interrupted by the volcanic structure of Cuma Mount, whose altitude reaches approximately 100 m a.s.l..

From the hydrogeological point of view, the regional groundwater flow system is unitary (Celico et al., 1992; Allocca et al., 2007), east-west oriented, toward the coastline (Fig. 1b). The same system is locally influenced by many interacting factors, as the hydraulic heterogeneity of volcanic-sedimentary succession, groundwater pumping, groundwater-drainage channel system and intrusion of seawater into groundwater system.

Surface hydrography of the area is characterized by a drainage system of micro-channels, built during the various interventions of reclamation of the area, which transfers the surface and groundwater

Table 1
Characteristics of wells and boreholes.

Stations	Latitude (m) N UTM	Longitude (m) E UTM	Ground elevation (m a.s.l.)	Groundwater level (m a.s.l.)
P1	4,522,373,15	420,670,94	9.87	1.31
P2	4,522,279,84	420,680,70	11.75	1.63
P3	4,522,387,82	420,586,94	5.38	1.67
P4	4,522,682,00	420,422,94	1.58	1.07
P5	4,522,689,19	420,442,93	1.65	1.09
P6	4,522,712,05	420,384,19	1.66	− 0.37
P7	4,522,503,44	420,378,73	11.41	1.25
P8	4,522,682,08	420,511,80	1.74	0.24
P9	4,522,490,22	420,440,18	5.31	1.47
P10	4,522,671,31	420,681,36	4.61	3.3
P11	4,522,481,62	420,881,56	13.27	3.36
P12	4,521,641,32	420,471,92	22.54	n.d.
P13	4,522,685,57	620,448,78	1.57	0.96

toward a near pumping station, located at Licola village.

The climate is Mediterranean type, with hot dry summers and moderately cool and rainy winters. Mean annual air temperatures are in the range of approximately 13–15 °C. Rainfall regime is of a coastal and Mediterranean type, characterized by a principal maximum in autumn-winter and a minimum in the summer. The average annual rainfall is about 700 mm/y.

3. Material and methods

3.1. Hydrostratigraphic data

A 2D hydrostratigraphic model of the aquifer system was developed based on stratigraphic data of five, B1–B5, reported by Bravi et al., 2003, Nicotera, 1959, and piezometric data from 13 existing wells (P1–P13) (Fig. 1c) with variable depth between 0.5 and 80.0 m below the ground level, recorded in a GIS geodatabase (Table 1). Due to the different detail of the borehole data, a stratigraphic reinterpretation and terminological homogenization of the dataset was carried out. For each borehole and well, a vertical log of the hydraulic conductivity and its hydraulic conductivity was obtained by assigning a value of hydraulic conductivity to each stratigraphic lithofacies, according to lithological and textural characteristics of unconsolidated and consolidates deposits (Freeze and Cherry, 1979). This approach allowed to figure out the hydrogeological role (aquifer or aquitard/aquiclude) of the different sediment lithofacies and geological formations considering groundwater circulation.

3.2. Hydrogeological monitoring

In order to analyze the groundwater flow and spatio-temporal variation of the piezometric levels of the coastal aquifer, a groundwater monitoring network was reconstructed on an experimental area of about 1 km^2 inside the *Cumae* archaeological park (Fig. 1d). The piezometric levels were monitored from December 2013 to February 2015 (Table 1) in thirteen wells (P1–P13), 6 shallows-wells (P2, P4, P5, P6, P11, P13, up to 15 m depth), and 7 deep-wells (P1, P3, P7, P8, P9, P10, P12 up to 80 m depth). Monitoring was performed, with monthly frequency, by a water level indicator (BFK-100 model, PASI, Italy).

Ground elevations of the wells were measured by GPS techniques (K9 Series RTK, KOLIDA Instrument, China), and verified through the reconstruction of a Digital Elevation Model (DEM) derived by a LiDAR survey (http://sit.cittametropolitana.na.it/lidar.html) with 1×1 m^2 cells, implemented in a GIS environment.

Multi-temporal maps of groundwater table elevations were reconstructed by the kriging geostatistical method. Daily pluviometric time series recorded by Licola gauge station managed by Regional Civil Protection Agency were collected.

3.3. Sampling and analysis

3.3.1. Physical and chemical sampling and analysis

Fig. 1c shows the physico-chemical characterization of the groundwater over the same time spam and frequency.

A dynamic sampling was performed at wells P1, P3, P7, P8, P10 and P12, by an electromechanical pump, whereas a static sampling was adopted at wells P2, P4, P5, P6, P9, P11, and P13 by a bailer or directly by hand where it was possible. Well purging was done running the submersible pumps by a flow rate < 30 L min^{-1} until temperature, electrical conductivity and pH were stable. The evacuated flask and bailer were filled once, emptied, then filled again before taking samples. A portion of the bailer contents was discarded prior to sample collection. Samples from the flask and bailer were slowly poured directly into 1 L glassware and plastic bottles. Temperature (T, °C), pH, electrical conductivity (E.C., dS m^{-1}) were determined on site by a multiparametric profilator (Sea Bird Electronics 911 Plus CTD; Sea-Bird Electronics). Samples were held in refrigerated storage and sent to laboratory for the analysis of HCO_3^-, SO_4^{2-}, Cl^-, F^-, Ca^{2+}, Mg^{2+}, Na^+, K^+. The analytes were determined by ion chromatography, IC Metrohm 850 Professional. Cations were separated by a Metrosep C4 250/4.0 column using 3.0 mM HNO_3 as eluent and a flow rate of 0.9 mL/min, whereas anions by a Metrosep A supp7 250/40 column using 3.6 mM Na_2CO_3 as eluent at a flow rate of 0.7 mL/min. Limits of detection were in the range of 1 ppb. Glassware and plastic bottles used for sample treatment and storage were rinsed with 10% (v/v) HNO_3 and twice-distilled water before use. Water samples were analyzed in triplicate, and concentrations are the average of three replicates. For quality control purposes, thirty groundwater samples were chosen randomly among those taken from the wells. These were then spiked with a mixture of metal soluble salts in such a quantity as to nearly double the original concentration of metals in the sample. Then they were extracted as previously described. Mean recoveries ranged from 85 to 97%. Basic statistics, factor analysis and hierarchical cluster analysis were performed by STATISTICA 5 software (StatSoft Inc., Tulsa, OK, USA).

3.3.2. ^{222}Rn monitoring

The noble gas ^{222}Rn (radon) is a naturally occurring radioactive isotope (half-life = 3.8 days), a by-product of the ^{238}U natural decay chain and a direct product of α–disintegration of ^{226}Ra (half-life = 1620 years), which is ubiquitous in sedimentary rocks and granites. Radon gas is soluble in water and consequently the gas may be incorporated into groundwater flows (Tanner, 1980). Radon emanates from the volcanic deposits in which the aquifer resides, its transport taking place basically through the fissure network in the fractured system or from mantle degassing. The quantity of radon dissolved in groundwater depends on different factors such as the characteristics of the aquifer, water-rock interaction, water residence time within aquifer, rock's content of radium, mixing with different radon-bearing groundwater (Choubey and Ramola, 1997; Choubey et al., 1997). Radon half-life and its solubility have allowed the use of radon gas as a natural groundwater tracer to identify and quantify groundwater/surface waters interactions or to attempt to elucidate the type of rocks through which groundwater flow (Cook et al., 2003; Stellato et al., 2008; Schubert et al., 2011; Stellato et al., 2013; Alonso et al., 2015).

The ^{222}Rn specific activity was measured from April 2014 to February 2015 with monthly frequency. Samples for ^{222}Rn were collected according to the US Environmental Protection Agency's procedure modified by Belloni et al. (1995). Ten mL of water were taken by disposable plastic syringes in 20 mL glass vials filled in advance with 14 mL of Mineral Oil Scintillator (Packard). ^{222}Rn was determined by a Rack Beta Packard liquid scintillation counter at least three hours after the sampling to allow equilibrium conditions of ^{222}Rn with its

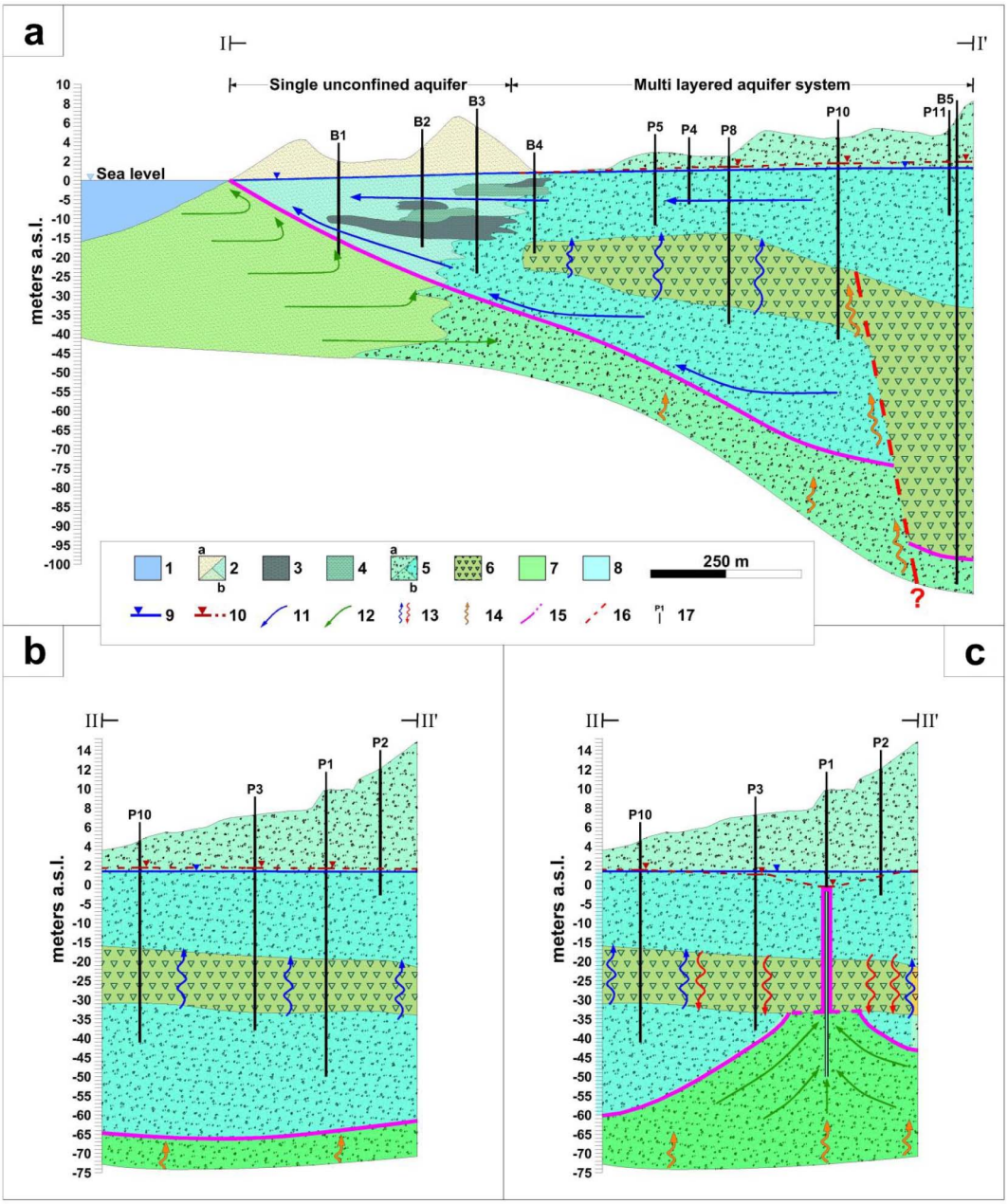

Fig. 3. 2D hydrostratigraphic model of the aquifer system, in static (a and b: February 2014) and pumping conditions (**c**: July 2014). 1) Seawater; 2) Sand (*aquifer*): (a) unsaturated (b) saturated of freshwater (c) saturated of saltwater; 3) Silt (*aquitard*); 4) Clay (*aquiclude*); 5) Pyroclastic silty sand (*aquifer*): (a) unsaturated (b) saturated of freshwater (c) saturated of saltwater; 6) Yellow Tuff (*aquiclude*); 7) Saltwater intrusion; 8) Freshwater; 9) Piezometric level of the shallow phreatic aquifer; 10) Potentiometric level of deep semi-confined aquifer, in static (**a** and **b**) (February 2014) and pumping conditions (**c**) (July 2014); 11) Groundwater flow direction; 12) Saline groundwater flow; 13) Vertical upward flow (blue) and downward flow (red); 14) Deep fluids rising; 15) Saltwater-freshwater interface estimated by Ghyben-Herzberg model; 16) Deep well (in square brackets: hydraulic head m a.s.l.); 17) Shallow well (in square brackets: hydraulic head m a.s.l.); 18) Borehole. (For interpretation of the references to color in this figure legend, the reader is referred to the web version of this article.)

daughters. Samples were counted for 15 min. Lower limit of detection was 1 Bq L^{-1}. Water samples were analyzed in triplicate, and concentrations are reported as the average of three replicates.

4. Results and discussion

4.1. Aquifer structure

Starting from the coastline landward (Fig. 3a), the seaside sector is characterized by marine and lacustrine sands (high permeability deposits) with intercalated low permeability horizons of silts (low permeability units) and clays (very low permeability units). This sector, from the coast line to approximately the B4 borehole (Fig. 3a), hosts a shallow unconfined aquifer, delimited at the bottom by the saltwater-freshwater interface. Laterally, in landward side, it is possible recognizing a multi-layered aquifer system, extending down to 80 m of depth (Fig. 3a). This is composed by a shallow unconfined aquifer, formed by volcaniclastic deposits, sandy-gravel in grain size (high permeability unit), and a deep semiconfined pyroclastic aquifer, down to the interface with YT horizon (low permeability semiconfining formation). This sector is characterized by very heterogeneous and anisotropic sediments, formed by unconsolidated volcanic-sedimentary deposits and interbedded consolidated horizons with lower permeability. Different piezometric heads were observed in the shallow and deep wells located into the multilayered aquifer system (Fig. 3a and b), indicating an upward vertical flow component, from the deep

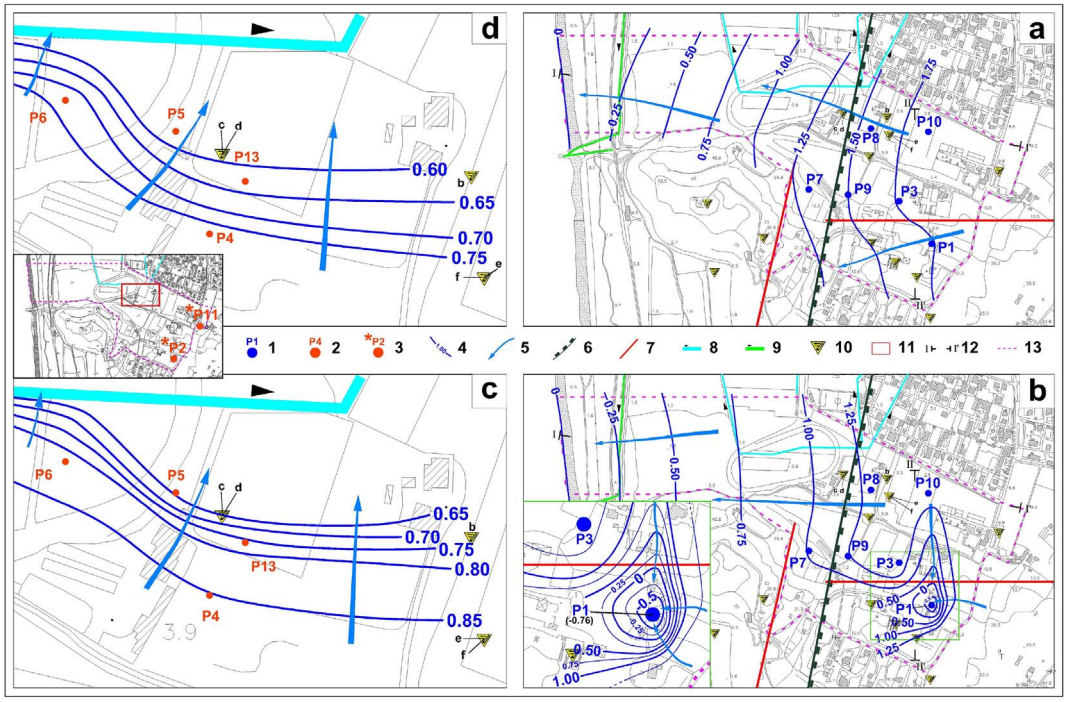

Fig. 4. Groundwater flow map of the study area for deep semi-confined aquifer (a and b) and shallow phreatic aquifer (c' and d') in February 2014 (a and d') and July 2014 (b and c'). (c and d): groundwater flow at local scale of the shallow phreatic aquifer in February 2014 (d) and July 2014 (c). 1) Deep well; 2) Shallow well; 3) Piezometric levels of the shallow well P2 (February 2014: + 1.76 m a.s.l.; July 2014: + 1.34 m a.s.l.) and P11 (February 2014: + 3.37 m a.s.l.; July 2014: + 3.21 m a.s.l.); 4) Piezometric contour line (m a.s.l.); 5) Groundwater flow direction; 6) CI caldera boundary; 7) Normal fault; 8) Groundwater draining channel; 9) Waste water channel; 10) Archaeological site; 11) Box of the Figs. c and d; 12) Hydrogeological section track of the Fig. 3; 13) Study area.

semiconfined pyroclastic aquifer to the shallow unconfined pyroclastic one. Given the seaward pinching out of the YT horizon, the two aquifers merge into a single one with a unique groundwater flow (Fig. 3a).

4.2. Groundwater flow

By the analysis of piezometric data, a conceptual groundwater flow model of deep and shallow aquifers were reconstructed (Fig. 4a, b, c, c', d and d'). In the case of the deep aquifer (Fig. 4a and b), the groundwater flow occurs through the pyroclastic deposits below the YT horizon (Fig. 3a and b). Due to the lower permeability of the latter, the deep aquifer is semiconfined (Fig. 3a and b), and it is fed by lateral groundwater flow coming from the north-western sector of the Phlegraean Fields volcanic aquifer (Fig. 1c), according to regional groundwater path observed at the basin scale (Celico et al., 1992; Allocca et al., 2007). During the recharge period (Fig. 4a) and lack of pumping, the piezometric contour pattern shows a groundwater flow oriented westward, with a principal groundwater drainage axis oriented toward the coastline and a groundwater divide passing through the Mount of Cuma. The piezometric head varies between 0.00 and 1.75 m a.s.l. (Fig. 4a) with values of the piezometric gradient around 2.0×10^{-3}. In the recession period (Fig. 4b), significant modifications were observed in the groundwater flow due to well pumping. A significant depression of hydraulic heads was observed, down to − 0.76 (P1 in Figs. 3c, 4b and 5) and − 2.3 m a.s.l. (P3, showed in Fig. 5), with flow lines oriented toward P1 (Figs. 3c and 4b), indicating the saltwater intrusion, due to the upcoming of freshwater-seawater interface (Figs. 3c and 4b).

In the case of the shallow aquifer (Fig. 4c' and d'), groundwater flow occurs in the pyroclastic deposits above the YT horizon, or in the coastal sands, where the YT horizon is absent (Fig. 3a and b). The shallow aquifer is unconfined, and during the recharge and recession periods it shows a general groundwater flow oriented westward (Fig. 4c' and d'), but at local scale an action of drainage by the micro-channels exists, with a local deviation of the groundwater flow northward oriented (Fig. 4c and d). This aquifer is recharged also by lateral groundwater flow from the north-western sector of the Phlegraean Fields volcanic aquifer (Fig. 1b). The piezometric head varies between 0.00 and 3.00 m a.s.l. (Fig. 4c' and d'), with a mean hydraulic gradient of about 2.70×10^{-3}. No variations of the piezometric head were caused by pumping (Figs. 4c', d' and 5).

In sector of P4-P5-P6-P13 wells (Fig. 4c and d), the gap of hydraulic head between the deep and shallow aquifers was assessed varying between 0.15 m and 0.65 m, causing an upward oriented groundwater flow.

4.3. Physical and chemical features of the groundwater and ^{222}Rn specific activity

4.3.1. Physical and chemical features

Table 2 displays the results of the chemical and physico-chemical characterization of the superficial and deep aquifer. Based on the mean annual temperature the groundwater can be mainly classified as cold, i.e. < 20.0 °C, and just for site P10 as hypothermal, i.e. in the range 20.0–35.0 °C (Schoeller, 1962). On the overall, pH values were in the slightly alkaline range, 7.07–8.15, with higher mean values for deep waters, 7.60. E.C. mean values displayed a wide difference between superficial and deep water, 1.211 vs 1.538 dS m^{-1}, with peaks above 2.000 dS m^{-1} for wells P1 and P9. These values and those derived of total salinity allowed to discriminate two different groups of groundwater, a group with medium mineral content, P2, P10, P11, P12 and P13 and another one with higher saline content, P1, P3, P4, P5, P6, P7, P8, and P9.

The hydrochemical data from most wells generally indicated low concentrations of major, Ca^{2+} and Mg^{2+}, and minor constituents, Na^{+}, K^{+}, with values practically matching between deep and superficial waters, with the exception of Na^{+} which showed higher mean loads by depth, 245 vs 148 mg L^{-1} and Cl^{-}, 265 vs 180 mg L^{-1}. Thus, these values were consistent with the already described values of E.C. The

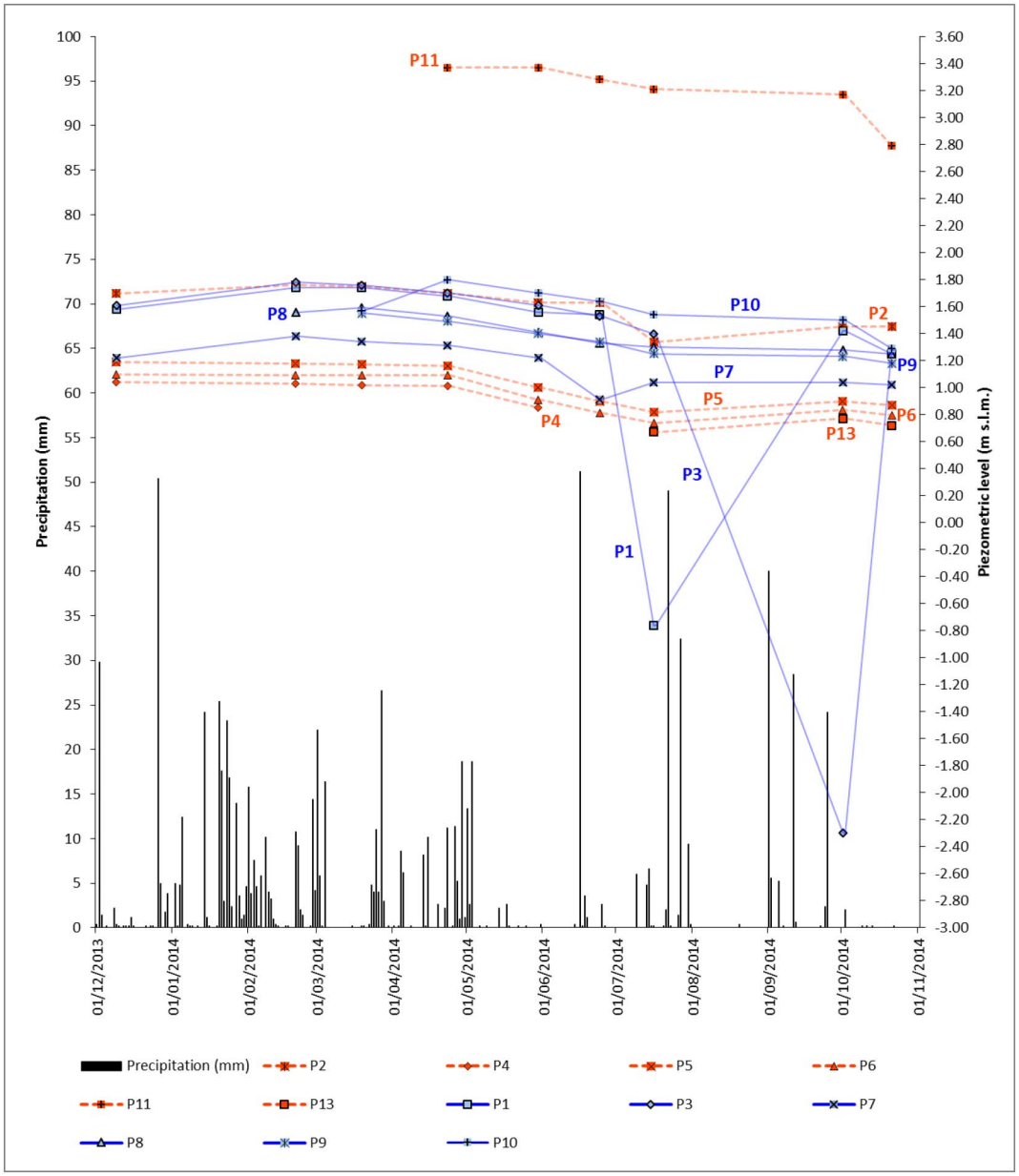

Fig. 5. Piezometric levels monitoring of shallow (red) and deep (blue) wells. The pink dashed line is the mean altitude (m a.s.l.) of archaeological ruins impacted. (For interpretation of the references to colour in this figure legend, the reader is referred to the web version of this article.)

entire set of hydrochemical data also revealed the wide temporal/spatial variability of the features of the aquifer. In fact, specific conductance ranged from ~0.541 dS m^{-1} at inland location, P2, to > 1.700 dS m^{-1} at sites where groundwater withdrawal rate for intensive crop irrigation or proximity to the coastal area allow saltwater intrusion, P1, P3 and P9, (Fig. 1c) locations where peaks of Cl^-, 384, 310 and 472 mg L^{-1} were observed. These salinity peaks were consistent with the depression cones due to intense pumping for agricultural activities during the recession phase (Fig. 4a). Outstanding levels of F^- were observed, in excess of the regulation limit of 1.5 mg L^{-1}. The F^- mean values at superficial aquifer was of 3.3 mg L^{-1} whereas at the deep aquifer was of 6.4 mg L^{-1}, being up to six-fold the regulation limit in the case of well P8, 8.6 mg L^{-1}. Only at P2 the mean level of F^-, 0.1 mg L^{-1}, was largely below the limit. These high levels were consistent with those (3.6–15.0 mg L^{-1}) reported by Celico et al. (1992) and Ducci and Sellerino (2012) for Phlegrean Fields. This might be attributable to the lithological features of the aquifers, constituted by volcanic and pyroclastic rocks, and the strong interaction between groundwater and localized rise of deep magmatic fluids highly mineralized.

In order to compare and correlate the different analyzed groundwater, the diagrams of Piper (Fig. 6) were elaborated, which also show changes over time of the major hydrochemical facies. The Piper diagrams clearly showed how the groundwater belongs in most cases to the Cl^--SO_4^{2-}-Na-K facies, except P2 which was merely HCO_3^--Ca-Mg, P3 and P12, HCO_3^--Na-K. The facies Cl^--SO_4^{2-}-Na-K characterizes the multilayer aquifer with some exception which were more evident in the deep waters, with presence of Cl^--SO_4^{2-}-Ca-Mg and HCO_3^--Na-K facies. The diagrams evidenced an elevated variability of the hydrogeochemical characteristics of the aquifers even though the area was of a very limited spatial extension. This was the case of P12 which evolved to the HCO_3^--Ca-Mg facies in May and June 2014. Another interesting temporal shift was showed by P7 which moves from the facies Cl^--SO_4^{2-}-Na-K to HCO_3^--Na-K in October 2014. But the most unstable well was P1, which belongs to Cl^--SO_4^{2-}-Na-K and Cl^--SO_4^{2-}-Ca-Mg during the months of more intensive crop irrigation and to HCO_3^--Ca-

Table 2
Results of physical and chemical analysis (mg L^{-1}); first row represents mean ± standard deviation.

Site	Temperature °C	pH	E. C. dS m^{-1}	Ca^{2+}	Mg^{2+}	Na^{+}	K^{+}	HCO_3^{-}	SO_4^{2-}	Cl^{-}	F^{-}	^{222}Rn Bq L^{-1}
P1	19.3 ± 1.0	7.20 ± 0.09	2.031 ± 0.420	209 ± 46	28.2 ± 4.0	200 ± 133	80.1 ± 6.3	673 ± 545	112.9 ± 15.9	384 ± 156	2.6 ± 1.9	41.6 ± 11.2
Rsd%	5.24	1.24	20.7	22	14.2	66.5	7.92	81.0	14.1	40.6	7.5	26.9
Min-max	18.0–21.0	7.04–7.35	1.631–3.070	144–331	24.0–37.0	85–434	71.4–89.6	305–2031	90.7–134.0	276–771	0.1–5.6	16.2–52.8
P2	18.4 ± 1.8	7.34 ± 0.18	0.541 ± 0.121	61 ± 15	7.5 ± 2.1	28.8 ± 10.3	50.7 ± 10.6	357 ± 168	15.7 ± 8.6	47 ± 30	0.1 ± 0.1	0.2 ± 0.4
Rsd%	10.1	2.39	22.4	24	28.4	35.7	20.9	47.1	55.1	64.7	62	n.d.
Min-max	15.5–20.5	7.21–7.70	0.375–0.694	38–74	4.4–10.1	16.5–43.3	36.5–65.6	200–616	8.4–30.0	26–107	0.1–0.2	n.d.
P3	18.8 ± 1.5	7.30 ± 0.27	1.800 ± 1.523	131 ± 49	25.9 ± 28.6	292 ± 346	65.0 ± 27.2	601 ± 206	49.3 ± 20.9	310 ± 468	3.4 ± 2.3	20.9 ± 20.2
Rsd%	8.1	3.73	84.6	37	110	119	41.7	34.3	42.3	151	67	96.6
Min-max	16.9–21.8	6.83–7.73	0.871–5.930	87–221	10.7–95.4	79–1060	43.1–125.4	383–1055	24.4–83.9	65.9–1632	0.7–7.0	5.7–48.9
P4	17.2 ± 6.2	7.86 ± 0.42	1.339 ± 0.113	102 ± 29	15.5 ± 1.0	162 ± 17	49.1 ± 5.8	532 ± 306	80.2 ± 7.2	232 ± 23	2.8 ± 1.3	8.0 ± 0.2
Rsd%	35.9	5.37	8.44	28	6.73	10.3	11.9	57.4	8.92	10.1	45	n.d.
Min-max	9.0–25.9	7.34–8.53	1.145–1.499	66–144	13.8–17.7	138–182	41.6–57.3	289–1049	67.2–89.8	200–271	0.3–3.9	n.d.
P5	16.9 ± 1.3	7.41 ± 0.29	1.485 ± 0.288	138 ± 66	18.8 ± 7.6	194 ± 37	59.6 ± 5.7	662 ± 602	90.3 ± 14.7	240 ± 70	4.4 ± 0.1	6.8 ± 3.0
Rsd%	7.6	3.95	19.4	47	40.2	19.1	9.64	91.0	16.3	29.1	3	44.1
Min-max	15.5–19.4	7.22–8.3	1.110–2.180	56–299	14.0–41.0	155–299	46.4–69.8	274–2501	73.7–126.0	200–451	4.1–4.5	2.2–13.7
P6	15.5 ± 3.5	7.61 ± 0.16	1.602 ± 0.137	106 ± 28	15.2 ± 2.4	249 ± 30	58.9 ± 6.5	532 ± 159	79.4 ± 10.8	268 ± 31	6.3 ± 0.6	1.7 ± 0.7
Rsd%	22.6	2.05	8.57	26	15.9	11.9	11.0	29.9	13.7	11.7	9	41.2
Min-max	11.5–20.2	7.40–8.00	1.366–1.808	74–153	12.1–18.7	183–289	50.1–70.7	342–927	63.5–101.5	209–306	5.4–7.0	1.1–8.9
P7	19.3 ± 1.1	7.57 ± 0.17	1.430 ± 0.069	71 ± 22	13.6 ± 1.3	226 ± 5	53.6 ± 2.6	490 ± 253	80.1 ± 6.24	237 ± 7	6.2 ± 0.6	72.0 ± 8.2
Rsd%	5.83	2.24	4.81	31	9.31	2.23	4.84	51.7	7.80	2.83	10	11.4
Min-max	18.0–22.0	7.43–8.00	1.340–1.611	43–124	12.4–16.5	218–234	49.4–57.3	328–895	70.3–88.6	222–249	4.8–6.8	63.4–86.8
P8	19.5 ± 1.1	8.15 ± 0.07	1.364 ± 0.049	50 ± 24	6.3 ± 2.1	272 ± 8	39.5 ± 1.5	375 ± 57	75.6 ± 3.7	229 ± 10	9.2 ± 0.2	8.4 ± 1.8
Rsd%	5.77	0.91	3.60	48	32.7	2.77	3.90	15.1	4.92	4.57	2	21.4
Min-max	17.9–21.4	8.04–8.30	1.290–1.468	25–84	3.6–9.5	261–282	37.1–42.9	302–530	70.5–81.0	205–240	8.8–9.4	5.8–15.6
P9	19.8 ± 1.2	7.71 ± 0.35	2.181 ± 0.302	80 ± 38	18.1 ± 6.6	391 ± 49	59.1 ± 8.2	562 ± 261	69.7 ± 6.5	472 ± 91	8.6 ± 0.5	16.5 ± 13.4
Rsd%	5.98	4.51	13.9	48	36.3	12.6	13.8	46.6	9.36	19.3	5	81.2
Min-max	17.8–21.8	7.37–8.50	1.375–2.410	27–154	5.2–28.8	269–438	39.2–66.2	365–1085	58.4–76.5	228–551	7.4–8.9	4.4–34.7
P10	20.6 ± 3.4	7.78 ± 0.16	1.129 ± 0.067	33 ± 11	4.8 ± 1.0	212 ± 12	38.3 ± 1.3	339 ± 29	91.2 ± 3.1	152 ± 10	8.2 ± 0.6	24.8 ± 5.5
Rsd%	16.3	2.01	6.0	34	20.6	5.58	3.46	8.50	3.45	6.54	7	22.2
Min-max	14.2–25.5	7.40–8.00	1.040–1.259	24–61	3.9–6.5	185–223	35.8–40.0	298–396	86.4–95.5	127–163	6.9–8.6	19.2–35.0
P11	17.6 ± 1.4	7.07 ± 0.19	1.108 ± 0.071	94 ± 19	17.5 ± 1.4	119 ± 3	44.9 ± 2.7	448 ± 340	132.2 ± 4.8	96 ± 4	2.3 ± 0.2	6.9 ± 0.6
Rsd%	7.75	2.64	6.36	20	8.13	2.39	5.96	75.9	3.60	3.86	8	8.6
Min-max	15.7–19.7	6.88–7.50	1.030–1.280	79–138	16.0–20.6	114–122	41.8–48.5	233–1061	128–140	90–101	1.9–2.4	3.8–7.7
P12	19.68 ± 1.22	7.50 ± 0.30	0.829 ± 0.267	62 ± 30	10.1 ± 5.2	119 ± 86	21.2 ± 13.0	339 ± 43	69.8 ± 46.1	71 ± 47	6.8 ± 5.2	47.8 ± 0.6
Rsd%	6.18	4.02	32.2	48	51.5	72.2	61.2	12.8	66.0	66.9	77	1.2
Min-max	17.9–21.3	6.90–7.75	0.423–1.030	33–101	5.5–18.1	8–182	4.1–30.8	292–429	9.8–102.3	10–102	0.1–10.6	46.8–47.8
P13	18.4 ± 4.5	7.55 ± 0.26	1.190 ± 0.320	115 ± 6	14.8 ± 6.6	137 ± 41	45.8 ± 15.1	523 ± 262	71.1 ± 26.6	197 ± 67	3.6 ± 0.4	n.d.
Rsd%	24.7	3.45	26.9	6	44.4	30.1	33.1	50.0	37.4	33.9	12	
Min-max	12.7–22.8	7.22–7.90	0.626–1.407	6–22	6.0–21.9	76–168	23.7–57.2	318–957	32.1–91.8	83–248	3.0–4.0	

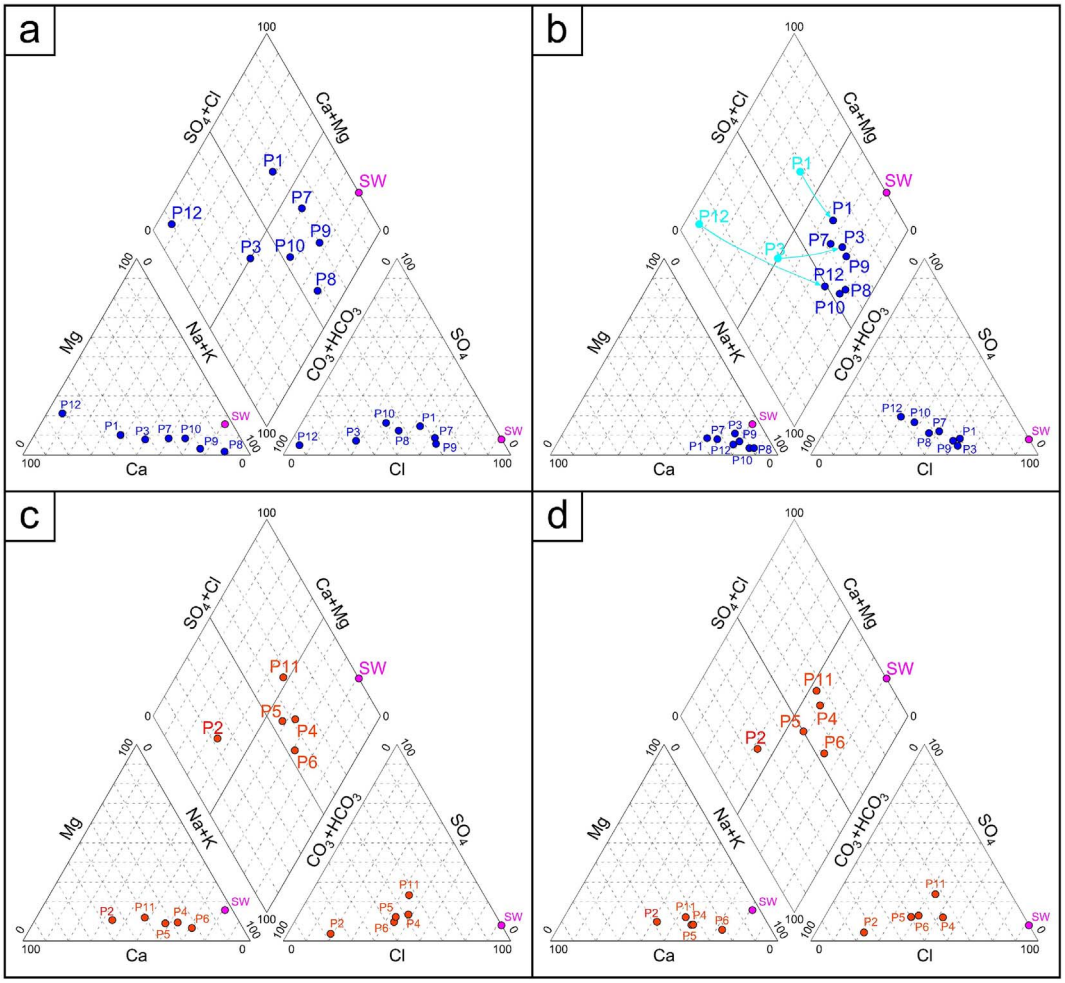

Fig. 6. Piper diagrams of groundwater sampled for the deep semi-confined aquifer (a and b) and for the shallow phreatic aquifer (c and d) in February 2014 (a and d) and July 2014 (b and c). SW indicates seawater. In light blue (b) the shifts from the recharge to the recession period. (For interpretation of the references to colour in this figure legend, the reader is referred to the web version of this article.)

Mg merely in February 2014.

These shifts were showed in Fig. 6 outlining the influence of pumping and rainfall intensity on the chemistry of groundwater. Hence, the overall data evidenced how the coastal aquifer was influenced by saltwater intrusion induced also by over-pumping as in the case of well P1. These results impact the health state of the archaeological site. In fact, whereas the already excavated ruins are affected by flooding during raining seasons, the buried monuments appear seriously threatened by the high load of SO_4^{2-} characterizing the observed dominant hydrochemical facies, i.e. Cl^--SO_4^{2-}-Na-K and by the high temporal variability of the hydro chemical features. The sulfation of carbonate (Sabbioni, 2003) makes the stones more fragiles which eventually undergo dissolution. The second process also severely damages the monuments because they live a permanent chemical instability.

4.3.2. ^{222}Rn specific activities

In Table 2 mean ^{222}Rn specific activities values, ranges and variation coefficients were reported. In shallow wells mean activity was 5.4 Bq $L^{-1}$with a range of 0.2–8.0 Bq L^{-1} whereas in deep wells was 31.5 Bq L^{-1} with a range of 8.4–72.0 Bq L^{-1}. The radon concentrations were comparable with variations reported from recently published studies for geothermal waters (Belgacem et al., 2015). This was the case of the concentration ranges reported for thermal baths of Denizli, Turkey, 0.67–25.9 Bq L^{-1} (Gurler et al., 2010), the touristic city of Sarein in Iran 0.212–3.89 Bq L^{-1} (Jalili-Radon activities in the thermal baths of Bursa, Turkey, 2.513–82.553 Bq L^{-1} (Gurler et al., 2010) were comparable with radon range measured in Cuma deep waters.

The higher ^{222}Rn specific activities measured in several deep wells with respect to shallow ones can be attributed to a longer residence time of groundwater, to the aquifer's rocks typology (i.e., content of ^{222}Rn parent nuclides ^{238}U and ^{226}Ra) and localized rise of gases and highly mineralized deep magmatic fluids along buried normal faults and deep fractured zones of the western edge of CI caldera. In particular, the highest ^{222}Rn specific activities were measured in the well P7 (72.0 ± 8.2 Bq L^{-1}) which is located in the proximity of a normal fault (see Fig. 1c) suggesting a possible localized contribution of volcanic gases and the rise of deep magmatic fluids enriching the groundwater radon content (Choubey et al., 2001; Vishal et al., 2011) or differences in lithology of the aquifer (see Section 3.3.2).

Fig. 7 shows the ^{222}Rn specific activities and the EC measured in deep (a) and shallow (b) wells in the recharge (April 2014) and the recession (July 2014) phases. As already observed in Fig. 5, significant differences were observed: both EC and ^{222}Rn specific activity of shallow wells were constant over time and space with average annual values of 1.17 ± 0.45 dS cm^{-1} and 5.4 ± 3.8 Bq L^{-1}, respectively; while deep wells were characterized by more variable signals. In particular, a significant seasonal trend can be observed in the wells P1 and P3. In fact, the lowest values were measured during the recharge phase while the highest were measured in the recession. These data further support the hypothesis that in the recession phase the increase in well pumping in P1 and P3 for irrigation purposes enables the abstraction of deeper and slowly circulating groundwater characterized by a

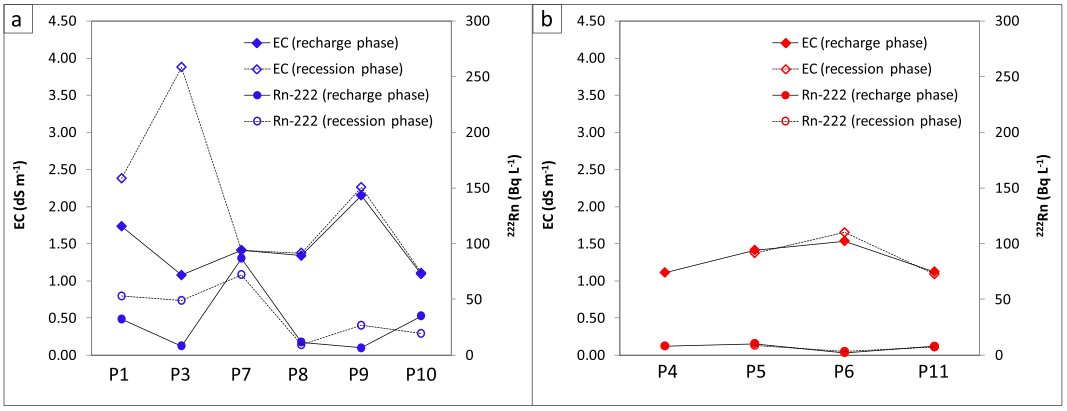

Fig. 7. ^{222}Rn specific activity and EC in deep (a) and shallow (b) wells in April (recharge phase) and July (recession phase) 2014.

significantly higher radon signal, especially. During the recharge phase, the radon signal in groundwater was lower likely due to the contribution of fast circulating groundwater (residence time < 30 days) and/or mixing with groundwater having a lower radon content. In the well P7 both the ^{222}Rn specific activity and the EC were very stable along the hydrologic year (CV < 15% and < 5%, respectively, see also Table 2). In particular, the radon constant values suggest that the aquifer's rock composition is rather homogeneous in the portion intercepted by the well P7 (see Section 3.3.2). Moreover, the stability of EC evidences that the deep aquifer in that area is not affected by seasonal changes.

4.3.3. Statistical analysis

Factor analysis led to grouping of different water quality parameters into three factors that explained over 80% of total variability in the observed distribution of water quality parameters, Table 3. Factor 1, accounting for about 45.6% of the total variance, consisted of high positive loadings of E.C., Ca^{2+}, Mg^{2+}, K^{+}, HCO_3^{-}, Cl^{-} which confirm the above observed strong influence of the marine intrusion. High positive loadings of F^{-} (0.94) and Na^{+} (0.73) for factor two, accounting for about 25.2% of the total variance, indicated weathering of volcanic ash deposits (Hudak and Sanmanee, 2003). High F^{-} can also occur from weathering and ion-exchange (F^{-}/OH^{-}) processes within the marine clays in the down dip regions that have higher groundwater residence times (Battaleb-Looie et al., 2012). Hudak (1999) attributed high levels of F^{-} in aquifer to ion exchange processes associated with deep regional groundwater flow and pumping-induced seepage from adjacent marine formation that are rich in various species including F^{-}. In the end, factor 3 accounted for about 11.0% of the total variance and consisted of high positive loading of SO_4^{2-} (0.72), revealing a significant role of this ion in groundwater salinization.

Table 3
Factor loadings and % of variance explained. Bold values indicate significance at $p = 0.05$.

Parameters	Factor 1	Factor 2	Factor 3
Well depth	− 0.55	0.09	0.51
T	− 0.25	0.62	0.17
pH	− 0.04	0.56	− 0.69
EC	**0.91**	0.39	0.09
Ca^{2+}	**0.77**	− 0.41	0.33
Mg^{2+}	**0.84**	− 0.26	0.39
Na^{+}	0.61	**0.73**	− 0.14
K^{+}	**0.90**	− 0.26	− 0.04
HCO_3^{-}	**0.93**	− 0.21	0.10
SO_4^{2-}	0.24	0.12	**0.72**
Cl^{-}	**0.89**	0.41	− 0.07
F^{-}	− 0.08	**0.94**	− 0.09
% of variance explained	45.6	25.2	11.0
Cumulative variance explained	45.6	70.8	81.8

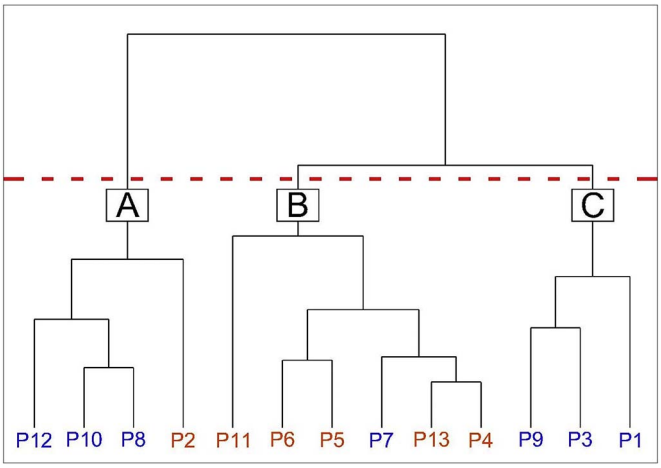

Fig. 8. Output of hierarchical cluster analysis (HCA). Letters indicate the clusters.

The hierarchical cluster analysis, performed by the criteria of Ward, allows to clearly recognise three main clusters (A, B and C), Fig. 8. Cluster A and C group deep wells whereas cluster B, with the exception of the well P7, groups superficial wells. It is interesting to note how clusters B and C are rather similar with shorter distance of link. This might be due to the different degree of groundwater withdrawal/replenishment and distribution of chemical species over time. Thus, wells appeared well characterized in regards to their depth and rate of utilization and recharge.

5. Conclusions

The study drew a first conceptual hydrogeological and hydrogeochemical model of the aquifer underlying the archaeological site and showed a marked complexity due to several interacting factors: sea proximity, volcanic nature of the site and anthropic pressure. Vertical and lateral lithological heterogeneity and coexistence of higher and lower permeability deposits made up the complexity of the volcanic-sedimentary coastal aquifer. The elevated spatial and temporal variability of the groundwater hydrochemistry was mainly due to pumping for agricultural practices which increased at higher depth the interaction between fresh and saline waters. Pumping during recharge and recession periods caused an unstable hydrochemistry with a dominant Cl^{-}-SO_4^{2-}-Na-K facies, and subordinately HCO_3^{-}-Ca-Mg and HCO_3^{-}-Na-K facies. Thus, we can conclude that the quality of groundwater resulted from marine seepage beside natural processes (e.g. mineral weathering and ion-exchange). However, volcanic rocks also affected the complexity of the system causing high loads of F^{-} and ^{222}Rn. This highlighted a strong interaction between groundwater and localized

rise along buried normal faults and deep fractured zones of the western edge of CI caldera boundaries of highly mineralized deep magmatic fluids. These particular features of the aquifer system do not allow to adopt the conventional practice to keep the monuments buried to slow down stone degradation. These results represent a first step of a hydrogeological and hydrogeochemical study aimed to perform further research to adopt appropriate reclamation strategies.

Acknowledgements

The authors wish to thank Dr. P. Caputo and Mr. C. Giordano of the Soprintendenza per i Beni Archeologici di Napoli (Cuma Office), for their collaboration for the development of the field groundwater monitoring at the archaeological site of *Cumae*.

References

Abdallah, I.M., Ebd El-Tawab, N.A., 2013. Effects of the groundwater on deterioration of the catacombs of Kom El-Shoqafa. Alexandria, Egypt. E-Conserv. 25, 169–181.
Allocca, V., Celico, P., 2008. Scenari idrodinamici nella piana ad Oriente di Napoli (Italia), nell'ultimo secolo: cause e problematiche idrogeologiche connesse. Giorn. Geol. Appl. 9, 175–198.
Allocca, V., Celico, F., Celico, P., De Vita, P., Fabbrocino, S., Mattia, S., Monacelli, G., Musilli, I., Piscopo, V., Scalise, A.R., Summa, G., Tranfaglia, G., 2007. Illustrative Notes of the Hydrogeological Map of Southern Italy. Istituto Poligrafico e Zecca dello Stato, Rome.
Allocca, V., Coda, S., De Vita, P., Iorio, A., Viola, R., 2016. Rising groundwater levels and impacts in urban and semirural areas around Naples (southern Italy). Rend. Online Soc. Geol. Ital. 41, 14–17.
Alonso, H., Cruz-Fuentes, T., Rubiano, J.G., González-Guerra, J., del Carmen Cabrera, M., Arnedo, M.A., Tejera, A., Rodríguez-Gonzalez, A., Pérez-Torrado, F.J., Martel, P., 2015. Radon in groundwater of the northeastern gran Canaria aquifer. Water. 7, 2575–2590.
Battaleb-Looie, S., Moore, F., Jacks, G., Ketabdari, M.R., 2012. Geological sources of fluoride and acceptable intake of fluoride in an endemic fluorosis area, southern Iran. Environ. Geochem. Health 34, 641–650.
de Beer, H., Matthiesen, H., 2008. Groundwater monitoring and modelling from an archaeological perspective: possibilities and challenges. In: Slagstad, T. (Ed.), Geology for Society, Geological Survey of Norway, Special Publication. 11. pp. 67–81.
Belgacem, A., Souid, F., Telahigue, F., Kharroubi, A., 2015. Temperature and radon-222 as tracer of groundwater flow: application to El Hamma geothermal aquifer system, southeastern Tunisia. Arab. J. Geosci. 8, 11161–11174.
Belloni, P., Cavaioli, M., Ingrao, G., Mancini, C., Notaro, M., Santaroni, P., Torri, G., Vasselli, R., 1995. Optimization and comparison of three different methods for the determination of Rn-222 in water. Sci. Total Environ. 173/174, 61–67.
Birolo, L., Tomeo, A., Trifuoggi, M., Auriemma, F., Paduano, L., Amoresano, A., Vinciguerra, R., De Rosa, C., Ferrara, L., Giarra, A., Luchini, A., De Maio, C., Greco, G., Vergara, A., 2016. A hypothesis on different technological solutions for outdoor and indoor Roman wall paintings. Archaeol. Anthropol. Sci. http://dx.doi.org/10.1007/s12520-016-0408-y.
Boardman, J., 1995. Les Grecs outre-mer: colonisation et commerce archaïque. Centre Jean Bérard, Paris.
Bravi, S., Fuscaldo, M., Guarino, P.M., Schiattarella, M., 2003. Evoluzione sedimentaria olocenica dell'area dell'antico Porto di Cumae (Campi Flegrei, Italia meridionale). In: Livadie, C.A., Ortolani, F. (Eds.), Variazioni climatico-ambientali ed impatto sull'uomo nell'area circum-mediterranea durante l'Olocene. Territorio storico ed ambiente. EdiPuglia, Bari, pp. 23–64.
Bucci, A., Naclerio, G., Allocca, V., Celico, P., Celico, F., 2011. Potential use of microbial community investigations to analyse hydrothermal systems behaviour: the case of Ischia Island, southern Italy. Hydrol. Proced. 25, 1866–1873.
Caputo, P., Morichi, R., Paone, R., 1996. Cuma e il suo parco archeologico. Un territorio e le sue testimonianze. Scienze e Lettere, Roma.
Celico, P., Dall'Aglio, M., Ghiara, M.R., Stanzione, D., Brondi, M., Prosperi, M., 1992. Geochemical monitoring of the thermal fluids in the Phlegraean Fields from 1970 to 1990. Boll. Soc. Geol. Ital. 111, 409–422.
Choubey, V.M., Ramola, R.C., 1997. Correlation between geology and radon levels in groundwater, soil and indoor air in Bhilangana Valley, Garhwal Himalaya, India. Environ. Geol. 32, 258–262.
Choubey, V.M., Sharma, K.K., Ramola, R.C., 1997. Geology of radon occurrence around Jari in Parvati Valley, Himachal Pradesh, India. J. Environ. Radioact. 34, 139–147.
Choubey, V.M., Bartarya, S.K., Saini, N.K., Ramola, R.C., 2001. Impact of geohydrology and neotectonic activity on radon concentration in groundwater of intermontane Doon Valley, outer Himalaya, India. Environ. Geol. 40, 257–266.
Cinque, A., Patacca, E., Scandone, P., Tozzi, M., 1993. Quaternary kinematic evolution of the southern Apennines. Relationships between surface geological features and deep lithospheric structures. Ann. Geophys. 36, 249–260.
Comte, J.C., Cassidy, R., Obando, J., Robins, N., Ibrahim, K., Melchioly, S., Mjemah, I., Shauri, H., Bourhane, A., Mohamed, I., Noe, C., Mwega, B., Makokha, M., Join, J.L., Banton, O., Davies, J., 2016. Challenges in groundwater resource management in coastal aquifers of East Africa: investigations and lessons learnt in the Comoros Islands, Kenya and Tanzania. J. Hydrol. Reg. Stud. 5, 179–199.
Cook, P.G., Favreau, G., Dighton, J.C., Tickell, S., 2003. Determining natural groundwater influx to a tropical river using radon, chlorofluorocarbons and ionic environmental tracers. J. Hydrol. 227, 74–88.
Deino, A.L., Orsi, G., Piochi, M., de Vita, S., 2004. The age of the Neapolitan Yellow Tuff caldera-forming eruption (Campi Flegrei caldera–Italy) assessed by 40Ar/39Ar dating method. J. Volcanol. Geotherm. Res. 133, 157–170.
Ducci, D., Sellerino, M., 2012. Natural background levels for some ions in groundwater of the Campania region (southern Italy). Environ. Earth Sci. 67, 683–693.
Fedele, L., Scarpati, C., Lanphere, M., Melluso, L., Morra, V., 2008. The Breccia Museo formation, Campi Flegrei, southern Italy: geochronology, chemostratigraphy and relationship with the Campanian Ignimbrite eruption. Bull. Volcanol. 70, 1189–1219.
Felisa, G., Ciriello, V., Di Federico, V., 2013. Saltwater intrusion in coastal aquifers: a primary case study along the Adriatic coast investigated within a probabilistic framework. Water. 5, 1830–1847.
Freeze, R.A., Cherry, J.A., 1979. Groundwater. Prentice-Hall, Englewood Cliffs, New Jersey.
Gurler, O., Akar, U., Kahraman, A., Yalcin, S., Kaynak, G., Gundogdu, O., 2010. Measurements of radon levels in thermal waters of Bursa, Turkey. Fresenius Environ. Bull. 19, 3013–3017.
Holden, J., Jared West, L., Howard, A.J., Maxfield, E., Panter, I., Oxley, J., 2006. Hydrological controls of in situ preservation of waterlogged archaeological deposits. Earth-Sci. Rev. 78, 59–83.
Hudak, P.F., 1999. Fluoride levels in Texas groundwater. J. Environ. Sci. Health A A34, 1659–1676.
Hudak, P.F., Sanmanee, S., 2003. Spatial patterns of nitrate, chloride, sulfate and fluoride concentrations in the Woodbine aquifer of north-central Texas. Environ. Monit. Assess. 82, 311–320.
Lambeck, K., Anzidei, M., Antonioli, F., Benini, A., Esposito, A., 2004. Sea level in Roman time in the Central Mediterranean and implications for recent change. Earth Planet. Sci. Lett. 224, 563–575.
Munzi, P., Brun, J.P., 2011. Cumes (Italie). Les fouilles du Centre Jean-Berard 2000–2010. Bull. Soc. Franç. Arch. Class. 51, 147–221 ((XLI, 2009-2010). Rev. Arch.).
Nicotera, P., 1959. Ricerche idrogeologiche nel distretto di Licola-Varcaturo (Napoli). Rivista Italiana di Geotecnica 1, 4–22.
Orsi, G., Di Vito, M., de Vita, S., 1996. The restless, resurgent Campi Flegrei Nested Caldera (Italy): constraints on its evolution and configuration. J. Volcanol. Geotherm. Res. 74, 179–214.
Rolandi, G., Bellucci, F., Heizler, M.T., Belkin, H.E., De Vivo, B., 2003. Tectonic controls on the genesis of ignimbrites from the Campanian volcanic zone, southern Italy. Mineral. Petrol. 79, 3–31.
Sabbioni, C., 2003. Mechanism of air pollution damage to stone. In: Brimblecombe, P. (Ed.), The Effects of Air Pollution on the Built Environment. Air Pollut. Rev. London Vol. 2. pp. 63–88.
Schoeller, H., 1962. Les eaux souterraines. Masson, Paris.
Schubert, M., Brueggemann, L., Knoeller, K., Schirmer, M., 2011. Using radon as an environmental tracer for estimating groundwater flow velocities in single well tests. Water Resour. Res. 47. http://dx.doi.org/10.1029/2010WR009572.
Stefaniuk, L., Morhange, C., Blanc, P.F., Francou, S., Goiran, J.P., 2005. Évolution des paysages littoraux dans la dépression sud-ouest de Cumes depuis 4000 ans. Méditerranée 104, 48–59.
Stellato, L., Petrella, E., Terrasi, F., Belloni, P., Belli, M., Sansone, U., Celico, F., 2008. Some limitations in using ^{222}Rn to assess river–groundwater interactions: the case of Castel di Sangro alluvial plain (central Italy). Hydrogeol. J. 16, 701–712.
Stellato, L., Terrasi, F., Marzaioli, F., Belli, M., Sansone, U., Celico, F., 2013. Is ^{222}Rn a suitable tracer of stream-groundwater interactions? A case study in central Italy. Appl. Geochem. 32, 108–117.
Tanner, A.B., 1980. Radon migration in the ground: a supplementary review. In: Gessel, T.F., Lowder, M.W. (Eds.), The Natural Radiation Environment. Proc. Symp. Houston, 1978, Rep., CONF-780422 III. United States Department of Energy, Washington, DC, pp. 5–56.
Todesco, M., Costa, A., Comastri, A., Colleoni, F., Spada, G., Quareni, F., 2014. Vertical ground displacement at Campi Flegrei (Italy) in the fifth century: Rapid subsidence driven by pore pressure drop. Geophys. Res. Lett. 41, 1471–1478.
Vishal, A., Singh, B.B., Surinder, S., 2011. Measurements of radon concentrations in ground water samples of tectonically active areas of Himachal Pradesh, North West Himalayas, India. Radiat. Prot. Environ. 34, 50–54.
Vitale, S., Isaia, R., 2014. Fractures and faults in volcanic rocks (Campi Flegrei, southern Italy): insight into volcano-tectonic processes. Int. J. Earth Sci. 103, 801–819.
De Vivo, B., Rolandi, G., Gans, P.B., Calvert, A., Bohrson, W.A., Spera, F.J., Belkin, A.E., 2001. New constraints on the pyroclastic eruption history of the Campanian volcanic plain (Italy). Mineral. Petrol. 73, 47–65.